Partial-moment minimum-entropy models for kinetic chemotaxis equations in one and two dimensions

Juliane Ritter[a], Axel Klar[b], Florian Schneider[c]

[a] *Fachbereich Mathematik, TU Kaiserslautern, Erwin-Schrödinger-Str., 67663 Kaiserslautern, Germany,* j_ritter@rhrk.uni-kl.de

[b] *Fachbereich Mathematik, TU Kaiserslautern, Erwin-Schrödinger-Str., 67663 Kaiserslautern, Germany,* klar@mathematik.uni-kl.de

[c] *Fachbereich Mathematik, TU Kaiserslautern, Erwin-Schrödinger-Str., 67663 Kaiserslautern, Germany,* schneider@mathematik.uni-kl.de

arXiv:1601.04482v1 [math.NA] 18 Jan 2016

Abstract

The aim of this work is to investigate the application of partial moment approximations to kinetic chemotaxis equations in one and two spatial dimensions. Starting with a kinetic equation for the cell densities we apply a half-/quarter-moments method with different closure relations to derive macroscopic equations. Appropriate numerical schemes are presented as well as numerical results for several test cases. The resulting solutions are compared to kinetic reference solutions and solutions computed using a full moment method with a linear superposition strategy.

Keywords: chemotaxis, moment models, minimum entropy

1. Introduction

The migration of cells is a complex process that is influenced by many factors such as external light, the pH or the oxygen concentration. In the following we concentrate on chemotaxis, the movement of cells in response to a chemical stimulus. A substance which causes cells to move in the direction of its gradient is called chemoattractant. The ideas of this work can easily be extended to chemorepellants, which have the opposite effect. Chemotaxis plays an important role in a lot of biological processes: It drives the movement of bacteria towards food and away from poisons or leads the sperm in the direction of the egg during fertilization. In multi-cellular organisms, it controls the guided accumulation of cells during embryological development and the movement of lymphocytes in the process of immunological response [2, 7, 32]. During cancer metastasis, mechanisms that allow chemotaxis can be subverted. Therefore a better understanding of the associated processes may lead to the development of novel therapeutic strategies. The movement of many bacteria, such as Escherichia coli which has been studied and described most intensely, is controlled by the alignment of their flagella, whip-shaped appendices with a rotary motor at their bases that are embedded in the cell membrane. Counter-clockwise rotation aligns the flagella, causing the bacterium to swim in a straight line ("run phase"); clockwise rotation causes the flagella to point in different directions, resulting in a movement on the spot ("tumble phase"). The latter re-orients the bacterium, so that overall we observe a random walk [1, 39]. A chemical stimulus influences the motion in the following way: if receptors sense that the bacterium is moving in the direction of the chemoattractant gradient, the "run phase" will be extended; if the concentration of the chemoattractant is decreasing in the direction of movement, it will be shortened. This results in a biased random walk [7]. Consideration of additional effects on the chemoattractant, such as production by the bacteria themselves, decay and diffusion, further increases the complexity of the model.

The original equations to model chemotaxis are the Keller-Segel equations. These equations and in particular, the properties of their solutions have been intensively investigated, see for example [5, 6, 10, 21, 23–25, 33]. For a survey and an extended reference list, see for example [3].

Our starting point is the classical kinetic chemotaxis equation [8]. Scaling it with the so called diffusive scaling leads to the Keller-Segel equation, see [8]. In general, the derivation of Keller-Segel type models, including flux-limited diffusion models and Fokker-Planck type models, from underlying kinetic or microscopic models is discussed for example in [3, 8, 9]. In particular, using moment closure approaches one may obtain macroscopic equations intermediate between kinetic and Keller-Segel equations, see the above mentioned references or [14, 23]. First order full moment equations with a linear closure function are sometimes called the Cattaneo equations. Applying maximum entropy closures one obtains improved first order full moment models [29]. Half- and quarter-moment closures have been developed for kinetic radiative transfer equations in [13, 16, 17]. It has been shown for these applications in various numerical experiments that the partial moment moment methods yields macroscopic models that can produce satisfying approximations. We refer to [16].

The aim of this work is to investigate the application of partial moment approximations to kinetic chemotaxis equations in one and two dimensions. Starting with a kinetic equation for the cell densities we apply a half- and quarter-moment method with varying closure relations to derive macroscopic equations in section 2. By applying numerical schemes that use certain properties of the moment systems and implementing it using Matlab [31], we obtain numerical results for several different test cases. Moreover, we compare the results to kinetic reference solutions and solutions computed using a full moment method and a linear superposition strategy. This work should be seen as a first step towards an efficient simulation strategy for kinetic chemotaxis equations via further refinement of the sphere, leading from a quarter moment model to a general first-order partial-moment model, which will hopefully converge to the true kinetic solution with a small number of refinements. This strategy should yield similiar results as higher order moment methods while being numerically much more efficient due to the inherent structur of the first order partial moment models.

2. Chemotaxis equations

The dynamics of chemotaxis can be modelled by the kinetic equations

$$\partial_t f + v \cdot \nabla_{\mathbf{x}} f = -\lambda(f - C_V \rho) + C_V \alpha \rho v \cdot \Phi(\nabla m) \tag{2.1}$$

$$\partial_t m - D_m \Delta m = \beta \cdot \rho - \delta m \tag{2.2}$$

where $f(t, \mathbf{x}, v)$ is the density of cells at time t and location $\mathbf{x} \in \mathbb{R}^d$, with velocity $v \in V$, whereas $\rho(t, \mathbf{x}) = \int_V f \, dv$ describes the overall density of cells at time t and location $\mathbf{x}$. $m(t, \mathbf{x})$ is the concentration of the chemoattractant at time t and location $\mathbf{x}$. V is the set of admissible velocities; since we assume that the cells move in arbitrary directions, but with constant speed, we have $V = S^2 = \{v \in \mathbb{R}^3 \mid \|v\|_2 = 1\}$ in three dimensions and consider the projections $V = [-1, 1]$ in one and $V = B_1(0) = \{v \in \mathbb{R}^2 \mid \|v\|_2 \leq 1\}$ in two dimensions [4]. The normalization constant C_V is determined by V: $C_V = \frac{1}{2}$ in one and $C_V = \frac{1}{4\pi}$ in two dimensions. The remaining coefficients characterize the biological system: λ and α describe the diffusivity and the chemotactic sensitivity of the cells. D_m is the diffusivity, β the production rate by the cells and δ the rate of chemical decay of the chemoattractant. The function Φ acts as a limiter for the influence of the chemoattractant gradient ∇m, which models the fact, that the "run phase" can only be extended to a certain extent. In the following we use

$$\Phi(\mathbf{x}) = \begin{cases} \left(\frac{\|\mathbf{x}\| - s}{\sqrt{1 + (\|\mathbf{x}\| - s)^2}} + s\right) \frac{\mathbf{x}}{\|\mathbf{x}\|} & \|\mathbf{x}\| \geq s \\ \mathbf{x} & \|\mathbf{x}\| \leq s \end{cases}$$

where the parameter $s \geq 0$ determines the extent of the limiting: $\max(\|\Phi(\mathbf{x})\|) \leq s+1$. Using this limiter in our simulation prevents blow up of the solution in finite time [11].

Assuming that $\lambda \geq C_V \alpha\,(s+1)$, the right-hand side of (2.1) can be written in the turning-kernel representation with non-negative kernel, which ensures that (2.1) admits a non-negative solution f [7].

We note that equation (2.1) is related via a diffusive scaling limit $t \to \epsilon^2 t$ and $x \to \epsilon x$ to a special case of the general Patlak-Keller-Segel

$$\partial_t \rho - \frac{1}{3\lambda}\Delta\rho = -\frac{\alpha}{3\lambda}\nabla\cdot(\rho\Phi(\nabla m))\ .$$

See [22] or [7] for details and rigorous proofs.

3. Moment models

In this section we introduce the method of moments and explore how it can be used to derive macroscopic equations from our kinetic equation (2.1). It can be seen as a Galerkin approximation in the velocity component v, by projecting the kinetic density $f(t,x,v)$ in v onto a finite-dimensional subspace of $L_2(V,\mathbb{R})$. Assume that this subspace is spanned by the basis $\mathbf{b}: V \to \mathbb{R}^n$, moments of f are defined as

$$\mathbf{u}(t,\mathbf{x}) = \int_V \mathbf{b}(v) f(t,\mathbf{x},v)\ dv =: \langle \mathbf{b} f\rangle\,,$$

where the integration is meant componentwise. Equations for $\mathbf{u}$ can be obtained by multiplying (2.1) with $\mathbf{b}$ and integrating over V, giving

$$\partial_t \mathbf{u} + \left\langle v\cdot\nabla_x \mathbf{b}\hat{f}\right\rangle = -\lambda(\mathbf{u} - C_V\rho\,\langle\mathbf{b}\rangle) + C_V\alpha\rho\,\langle v\cdot\Phi(\nabla m)\mathbf{b}\rangle\,. \tag{3.1}$$

Since the product of the components of v and $\mathbf{b}$ are generally not in the span of $\mathbf{b}$, the ansatz $\hat{f}$ has to be specified, determining the closure relation of (3.1). A typical example for $\mathbf{b}$ is the set of monomials in v, i.e. $\mathbf{b} = \left(1, v, v\otimes v, v^{\otimes 3}, \dots v^{\otimes n}\right)$, leading to what is commonly referred to as P_N and M_N models, depending on the choice of $\hat{f}$ [27, 29, 30]. Since full-moment models (i.e. integration over the whole velocity domain V) suffer from severe problems [20], we will focus on partial moment models, which build moments for partitions of V separately [13, 17, 35]. Since some of the derived models may contain unphysical negative densities ρ we replace (2.2) with

$$\partial_t m - D_m\Delta m = \beta\cdot\max(\rho,0) - \delta m.$$

This ensures that $m \geq 0$ is still guaranteed.

3.1. One dimension

Given a density function $f(t,x,v)$ with $t\in\mathbb{R}^+$, $x\in D\subset\mathbb{R}$ and $v\in V=[-1,1]$, we define the zeroth, first and second half-moments as

$$\rho_\pm(t,x) := \int_{V_\pm} f(t,x,v)dv,\quad q_\pm(t,x) := \int_{V_\pm} v f(t,x,v)dv,\quad r_\pm(t,x) := \int_{V_\pm} v^2 f(t,x,v)dv, \tag{3.2}$$

with $V_- := [-1,0]$, $V_+ := [0,1]$. Further assuming that $f\geq 0$, the monotonicity of the integral directly implies the sign restrictions $\rho_\pm \geq 0$, $\pm q_\pm \geq 0$ and $r_\pm \geq 0$. We can derive further properties for the normalized first and second half-moments

$$u_\pm := \frac{q_\pm}{\rho_\pm} \quad\text{and}\quad w_\pm := \frac{r_\pm}{\rho_\pm}\,.$$

Since $|v| \leq 1$ for all $v \in V$, we have

$$\rho_\pm = \int_{V_\pm} f dv \geq \int_{V_\pm} |v| f dv \geq \left| \int_{V_\pm} v f dv \right| = |q_\pm|.$$

Therefore $|u_\pm| \leq 1$, which implies $u_\pm \in V_\pm$ by using the sign restrictions. Additionally, we see

$$\pm q_\pm = \int_{V_\pm} v f dv \geq \int_{V_\pm} v^2 f dv = r_\pm \,.$$

Using the Cauchy-Schwartz inequality we also observe

$$q_\pm^2 = \left(\int_{V_\pm} v f dv \right)^2 \leq \left(\int_{V_\pm} v^2 f dv \right) \left(\int_{V_\pm} f dv \right) = r_\pm \rho_\pm.$$

Thus, the normalized second moments satisfy

$$u_\pm^2 \leq w_\pm \leq \pm u_\pm \,. \tag{3.3}$$

The relations derived above are necessary and sufficient for the existence of a non-negative density function f realizing a set of moments $\rho_\pm$, $q_\pm$ and $r_\pm$. For that reason they are also called realizability conditions. For a proof of sufficiency, see e.g. [12, 36]. In one dimension the kinetic equation (2.1) for the cell density f simplifies to

$$\partial_t f + v \partial_x f = -\lambda (f - \frac{1}{2}\rho) + \frac{1}{2} \alpha \rho v \phi(\partial_x m),$$

where we used $C_V = \left(\int_V 1 dv \right)^{-1} = \frac{1}{2}$.
Integrating over $V_\pm$ yields

$$\partial_t \rho_\pm + \partial_x q_\pm = \frac{\lambda}{2} \left(\rho_+ + \rho_- - 2\rho_\pm \right) + \frac{\alpha}{4} \left(\rho_+ + \rho_- \right) \Phi(\partial_x m). \tag{3.4}$$

Additionally, multiplication by v and integration over $V_\pm$ gives

$$\partial_t q_\pm + \partial_x r_\pm = \pm \frac{\lambda}{4} \left(\rho_+ + \rho_- \mp 4 q_\pm \right) + \frac{\alpha}{6} \left(\rho_+ + \rho_- \right) \Phi(\partial_x m). \tag{3.5}$$

Here, we used the obvious properties $\int_{V_\pm} 1 dv = 1$, $\int_{V_\pm} v dv = \pm \frac{1}{2}$, $\int_{V_\pm} v^2 dv = \frac{1}{3}$. This system of four partial differential equations (3.4)-(3.5) in six variables $\rho_\pm$, $q_\pm$ and $r_\pm$ is under-determined, requiring to derive closure relations $r_\pm = r_\pm(\rho_\pm, q_\pm)$.

3.1.1. Linear closure

A very cheap closure relation can by derived by using the linear ansatz

$$\hat{f}(t,x,v) = \begin{cases} a_+(t,x) + b_+(t,x) v & \text{if } v \in V_+, \\ a_-(t,x) + b_-(t,x) v & \text{if } v \in V_-. \end{cases}$$

Plugging this into (3.2) yields

$$r_\pm = -\frac{1}{6} \rho_\pm \mp q_\pm.$$

This simple closure relation can be implemented very easily but contradicts the realizability conditions (3.3) since e.g. for $\rho_\pm = 1$ and $q_\pm = 0$ it follows that $\rho_\pm r_\pm = -\frac{1}{6} < 0 = q_\pm^2$. Thus, the approximation will behave physically wrong (compared to the original kinetic equation) in these regimes, where the underlying ansatz is negative. This is similar to the case of the P_N equations, see e.g. [20, 26, 36]. This model will be called QP_1.

3.1.2. Minimum-entropy closure

The exponential ansatz

$$\hat{f}(t,x,v) = \begin{cases} \exp(a_+(t,x) + b_+(t,x)v) & \text{if } v \in V_+, \\ \exp(a_-(t,x) + b_-(t,x)v) & \text{if } v \in V_- \end{cases}$$

can be derived as the solution of the constrained minimization problem

$$\min \mathcal{H}(\hat{f}) = \left\langle \eta(\hat{f}) \right\rangle \tag{3.6}$$

under the moment constraints

$$\left\langle \mathbf{b}\hat{f} \right\rangle = \mathbf{u}, \tag{3.7}$$

where η is given by the Maxwell-Boltzmann entropy $\eta(\hat{f}) = \hat{f}\log\left(\hat{f}\right) - \hat{f}$ [29]. The basis is chosen to be $\mathbf{b} = \left(\mathbb{1}_{V_-}, v\mathbb{1}_{V_-}, \mathbb{1}_{V_+}, v\mathbb{1}_{V_+}\right)$ with the indicator function $\mathbb{1}$ on $V_\pm$. Again, calculating the moment integrals (3.2) for $\hat{f}$ yields the following relations for the normalized first and second half-moments:

$$u_\pm = \frac{q_\pm}{\rho_\pm} = \frac{(\pm b_\pm - 1)\exp(\pm b_\pm) + 1}{b_\pm(\exp(\pm b_\pm) - 1)},$$
$$w_\pm = \frac{r_\pm}{\rho_\pm} = \frac{(b_\pm^2 \mp 2b_\pm + 2)\exp(\pm b_\pm) - 2}{b_\pm^2(\exp(\pm b_\pm) - 1)}.$$

Since these expressions depend only on $b_\pm$, not on $a_\pm$, we can invert them numerically using tabulation, see e.g. [15, 18]. It is more computationally expensive than the linear closure relation, but satisfies the realizability conditions (3.3), see Figure 1. This model will be called QM_1.

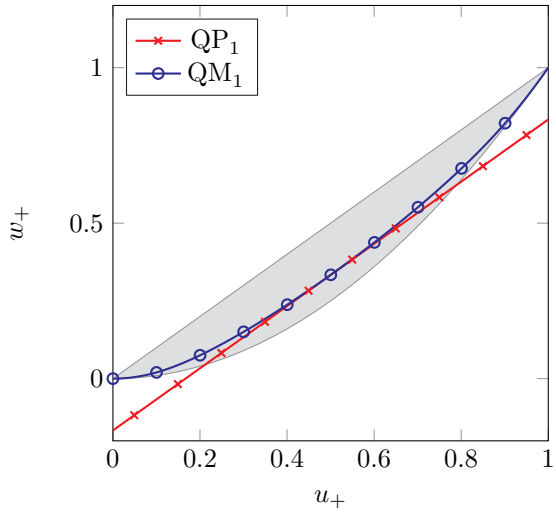

Figure 1: Comparison of different closure relations. The set of realizable moments is shown in grey.

3.2. Two dimensions

In this section the definitions and methods of the previous section are extended to two dimensions. Most calculations will work analogously. For a given density $f(t,\mathbf{x},v)$ with $t \in \mathbb{R}^+$, $\mathbf{x} := (x,y)^T \in D \subset \mathbb{R}^2$ and

$v := (v_x, v_y)^T \in V = B_1(0)$, we define quarter-moments up to second order as

$$\rho_{\pm\pm'}(t,\mathbf{x}) := \int_{V_{\pm\pm'}} f(t,\mathbf{x},v(\phi,r))d\phi dr =: \langle f\rangle_{\pm\pm'},$$
$$q_{\pm\pm'}(t,\mathbf{x}) := \int_{V_{\pm\pm'}} v(\phi,r)f(t,\mathbf{x},v(\phi,r))d\phi dr =: \begin{pmatrix} q^x_{\pm\pm'}(t,\mathbf{x}) \\ q^y_{\pm\pm'}(t,\mathbf{x}) \end{pmatrix},$$
$$r_{\pm\pm'}(t,\mathbf{x}) := \int_{V_{\pm\pm'}} v(\phi,r)\otimes v(\phi,r)f(t,\mathbf{x},v(\phi,r))d\phi dr =: \begin{pmatrix} r^{xx}_{\pm\pm'}(t,\mathbf{x}) & r^{xy}_{\pm\pm'}(t,\mathbf{x}) \\ r^{xy}_{\pm\pm'}(t,\mathbf{x}) & r^{yy}_{\pm\pm'}(t,\mathbf{x}) \end{pmatrix},$$

with $v(\phi,r) := (\sqrt{1-r^2}\cos(\phi), \sqrt{1-r^2}\sin(\phi))^T$ and $V_{++} := [-1,1]\times[0,\frac{\pi}{2}]$, $V_{-+} := [-1,1]\times[\frac{\pi}{2},\pi]$, $V_{--} := [-1,1]\times[\pi,\frac{3\pi}{2}]$ $V_{+-} := [-1,1]\times[\frac{3\pi}{2},2\pi]$. Again, normalized moments can be defined as

$$u_{\pm\pm'} := \frac{q_{\pm\pm'}}{\rho_{\pm\pm'}} \quad \text{and} \quad w_{\pm\pm'} := \frac{r_{\pm\pm'}}{\rho_{\pm\pm'}},$$

satisfying similar relations as in one dimension. For example, the first moment has to be located within the corresponding quarter sphere, i.e. $u_{\pm\pm'} \in v(V_{\pm\pm'})$ [16, 34, 38]. Equations for the moments $\mathbf{u}$ can be obtained by testing (2.1) with 1 and v, and integrating over the four quarter spheres $V_{\pm\pm'}$:

$$\partial_t\rho_{\pm\pm'} + \nabla\cdot q_{\pm\pm'} = \frac{\lambda}{4}(\rho - 4\rho_{\pm\pm'}) + \frac{1}{4\pi}\alpha\rho\langle v\rangle_{\pm\pm'}\cdot\Phi(\nabla m), \tag{3.8}$$
$$\partial_t q_{\pm\pm'} + \nabla\cdot r_{\pm\pm'} = \frac{\lambda}{8}(\rho - 8q_{\pm\pm'}) + \frac{1}{4\pi}\alpha\rho\langle v\otimes v\rangle_{\pm\pm'}\Phi(\nabla m). \tag{3.9}$$

The linear and minimum-entropy closures can be derived as in one dimension, using the anstze

$$\hat{f} = \begin{cases} a_{++} + b_{++}\cdot v & \text{if } (\phi,r)\in V_{++}, \\ a_{-+} + b_{-+}\cdot v & \text{if } (\phi,r)\in V_{-+}, \\ a_{--} + b_{--}\cdot v & \text{if } (\phi,r)\in V_{--}, \\ a_{+-} + b_{+-}\cdot v & \text{if } (\phi,r)\in V_{+-}, \ . \end{cases}$$

and

$$\hat{f} = \begin{cases} \exp(a_{++} + b_{++}\cdot v) & \text{if } (\phi,r)\in V_{++}, \\ \exp(a_{-+} + b_{-+}\cdot v) & \text{if } (\phi,r)\in V_{-+}, \\ \exp(a_{--} + b_{--}\cdot v) & \text{if } (\phi,r)\in V_{--}, \\ \exp(a_{+-} + b_{+-}\cdot v) & \text{if } (\phi,r)\in V_{+-}, \end{cases}$$

respectively. The minimum-entropy closure can be obtained again using a suitable two-dimensional table-lookup [16]. Its second moment is depicted in Figure 2.

4. Numerical scheme

The system of moment equations (3.1) is discretized using a first-order kinetic scheme on equidistant, structured grids (see e.g. [16, 19, 20, 37]). It is based on first discretizing (2.1) in space using the first-order Upwind scheme [40] and then use the method of moments in the velocity variable. In one dimension, the scheme has the following form, abusing $v \geq 0$ for $v \in V_+$ and $v \leq 0$ for $v \in V_-$:

$$\rho_+^{n+1,i} = \rho_+^{n,i} - \frac{\Delta t}{\Delta x}\left(q_+^{n,i} - q_+^{n,i-1}\right) + \Delta t\left(-\lambda\rho_+^{n,i} + \frac{1}{2}\lambda\rho^{n,i} + \frac{1}{4}\alpha\rho^{n,i}\Phi(\partial_x m)^{n,i}\right),$$
$$\rho_-^{n+1,i} = \rho_-^{n,i} - \frac{\Delta t}{\Delta x}\left(q_+^{n,i+1} - q_+^{n,i}\right) + \Delta t\left(-\lambda\rho_-^{n,i} + \frac{1}{2}\lambda\rho^{n,i} - \frac{1}{4}\alpha\rho^{n,i}\Phi(\partial_x m)^{n,i}\right),$$

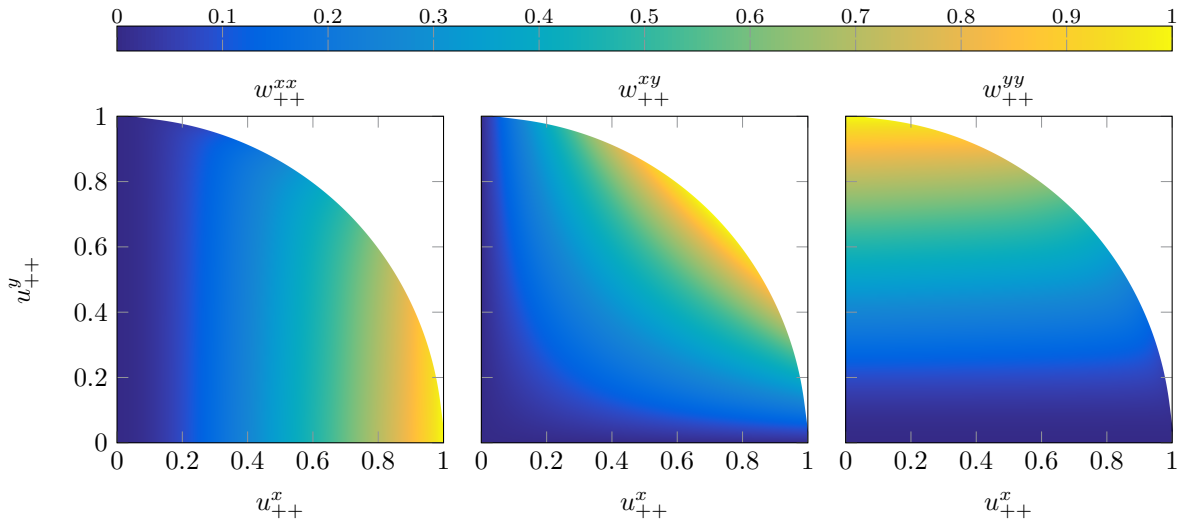

Figure 2: Quarter-moment minimum-entropy closure.

and

$$q_+^{n+1,i} = q_+^{n,i} - \frac{\Delta t}{\Delta x}\left(r_+^{n,i} - r_+^{n,i-1}\right) + \Delta t\left(-\lambda q_+^{n,i} + \frac{1}{4}\lambda\rho^{n,i} + \frac{1}{6}\alpha\rho^{n,i}\Phi(\partial_x m)^{n,i}\right),$$
$$q_-^{n+1,i} = q_-^{n,i} - \frac{\Delta t}{\Delta x}\left(r_+^{n,i+1} - r_+^{n,i}\right) + \Delta t\left(-\lambda q_-^{n,i} - \frac{1}{4}\lambda\rho^{n,i} + \frac{1}{6}\alpha\rho^{n,i}\Phi(\partial_x m)^{n,i}\right),$$

where $\rho_\pm^{0,i}$ and $q_\pm^{0,i}$ are the cell-averages of the initial conditions $\rho_\pm(0,x)$ and $q_\pm(0,x)$ in the i-th cell, respectively. The chemoattractant equation (2.2) is discretized using an implicit finite-difference approximation, yielding

$$m^{n+1,i} - D_m\frac{\Delta t}{\Delta x^2}(m^{n+1,i+1} - 2m^{n+1,i} + m^{n+1,i-1}) = \beta\rho + (1-\delta)\,m^{n,i}.$$

The occurring (large and sparse) linear system is solved using the stabilized bi-conjugate gradient method implemented in the Matlab [31] function `bicgstab`. Analogously, the scheme extends to two dimensions, performing the "upwinding" on the corresponding quarter moments. Details on this implementation can be found in [34]. We choose $\Delta t = \frac{0.5}{\frac{1}{\Delta x}+\lambda+\alpha(s+1)}$ in one dimension and $\Delta t = \frac{0.5}{\frac{1}{\min(\Delta x,\Delta y)}+\lambda+\alpha(s+1)}$ in two dimensions to ensure the stability of the scheme. Since it is essential to ensure the realizability conditions in case of the minimum-entropy closure (otherwise, the defining minimization problem has no solution), we use a projector into the set of realizable moments, as derived above. We set after each new calculation of $\rho_\pm$ and $q_\pm$:

$$\rho_\pm = \max(\rho_\pm, 10^{-14}),$$
$$q_\pm = \pm\max(\pm q_\pm, 0),$$
$$q_\pm = \begin{cases} q_\pm & \text{if } \|q_\pm\| \le 1, \\ \frac{q_\pm}{\|q_\pm\|} & \text{if } \|q_\pm\| > 1, \end{cases}$$

and analogously in two dimensions. Since we want to model the chemotaxis of cells in an isolated domain, we implement reflective boundary conditions for equation (2.1). Therefore we construct a layer of ghost cells, which are to be the neighbours of the boundary cells of the domain, and define their values before each step in the algorithm. In the one dimensional case we observe the following: Only those cells that are "travelling to the left" are reflected from the left boundary and afterwards "travel to the right". That means

only those cells with $v \in V_-$ are reflected on the left boundary and afterwards have $v \in V_+$. Conversely, only those cells with $v \in V_+$ are reflected from the right boundary to then have $v \in V_-$. Therefore we set:

$$\rho_+(\text{left ghost cells}) = \rho_-(\text{left boundary cells}),$$
$$\rho_-(\text{right ghost cells}) = \rho_+(\text{right boundary cells}),$$

and

$$q_+(\text{left ghost cells}) = -q_-(\text{left boundary cells}),$$
$$q_-(\text{right ghost cells}) = -q_+(\text{right boundary cells}) \ .$$

In two dimensions the idea remains the same, but we have two directions of reflection, see Figure 3. In all cases, the chemoattractant gets reflected from the boundary in an isotropic manner. Therefore

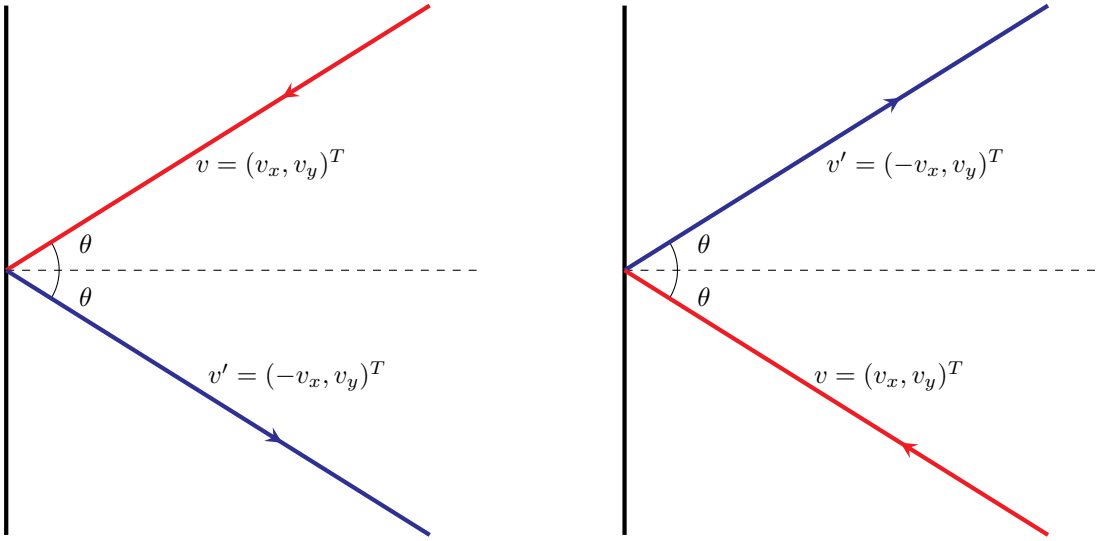

(a) $v = v(\phi, r)$ with $(\phi, r) \in V_{--}$ (b) $v = v(\phi, r)$ with $(\phi, r) \in V_{-+}$

Figure 3: Illustration of reflection at the left boundary

$m(Ghostcells) = m(Boundary)$. For Equation (2.2) we use Neumann boundary conditions, which can be implemented easily by defining the neighbours of the boundary to be themselves, e.g the left neighbours of the left boundary cells to be the left boundary cells.

5. Numerical experiments

To test the implemented scheme, we will submit it to a number of examples and compare the results to those computed with other means. We will also interpret the results in terms of our physical model of chemotaxis. All codes are implemented in Mathworks Matlab [31].

5.1. One dimension

In one dimension, we compare the results of our simulation to those computed by solving the kinetic equations (2.1) and (2.2) directly. For the latter, we used an implementation by Andreas Roth [1], which also

[1] TU Kaiserslautern, roth@mathematik.uni-kl.de

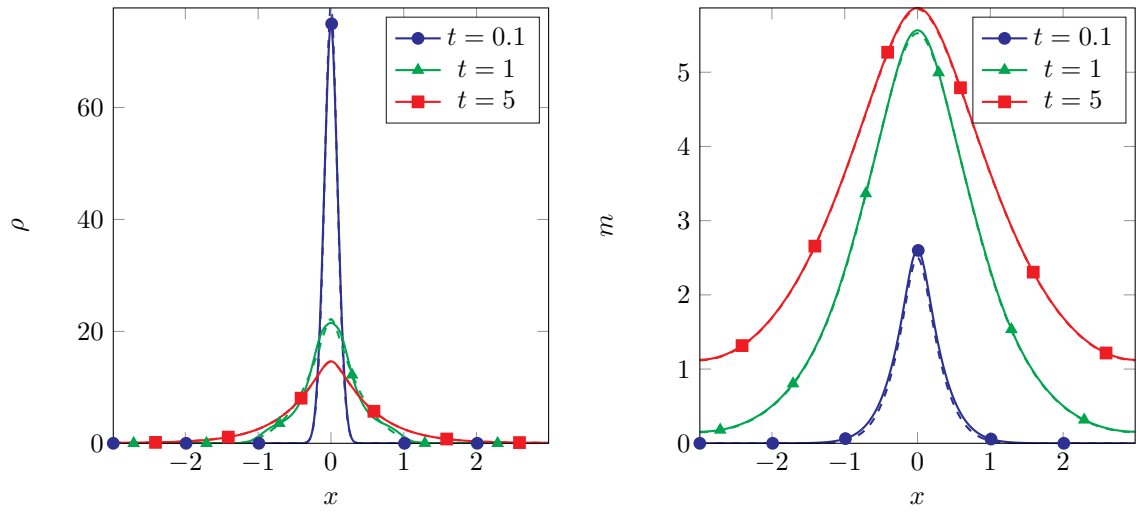

Figure 4: Half-moment minimum-entropy (solid with marks) and kinetic model (dashed) for the one-spike example.

uses the first-order Upwind scheme, but is explicit in the chemoattractant equation. Unless otherwise noted we will use isotropic initial conditions, which means $f(0, x, v) = f(0, x)$ and therefore

$$\rho_{\pm}(0, x) = \int_{V_{\pm}} f(0, x, v)dv = f(0, x) \ .$$

This implies

$$q_{\pm}(0, x) = \int_{V_{\pm}} vf(0, x, v)dv = \pm\frac{1}{2}f(0, x) = \pm\frac{1}{2}\rho_{\pm}(0, x).$$

5.1.1. One Spike

First, we simulate the effects of chemotaxis on an aggregation of cells in the centre of the domain in the absence of a chemoattractant initially. This is modelled by the initial data

$$\rho_{\pm}(0, x) = \frac{1}{2}\left(100 \exp\left(-\frac{x^2}{0.01}\right) + 10^{-4}\right)$$
$$m(0, x) = 0$$

on the domain $x \in [-3, 3]$ with the parameters $\alpha = 2$, $D_m = 1$, $\beta = 1$, $\delta = 1$, $\lambda = 2$ and $s = 0$.
Figure 4 shows, that the aggregation of ρ diffuses with decreasing speed, resulting in a "smeared out" version of the initial state. The concentration of the chemoattractant m first increases drastically until it matches ρ, which is caused by the production of the chemoattractant by the cells themselves, and then flattens out simultaneously with ρ. Varying the parameters confirms their physical interpretations supplied in the beginning: increasing the diffusivity D_m, λ speeds up the diffusion process and results in a more flattened out distribution, while increasing the parameters α or β leads to reciprocal reinforcing of the spiky distribution and therefore counteracts the diffusion.
When comparing the results obtained by using the different closure relations, one can only observe negligible differences, since the initial condition does not provoke negativity of ρ for the linear or fractional closures. Therefore we only consider the exponential closure in the following.
Most importantly, we see that the macroscopic and kinetic solutions behave very similarly. The minimum-entropy solution is slightly more diffusive, but with advancing time the deviation is negligible and almost

invisible to the naked eye. This shows that the macroscopic model yields very good results for this example while being much cheaper computationally: the kinetic reference solution has computation times [2] of 9.9s and 126.8s for $\Delta x = 0.1$ and $\Delta x = 0.02$ respectively with $T = 5$, whereas the macroscopic half-moment solution needs 1.0s and 3.3s with the exponential and 0.3s and 1.3s with the linear closure.

5.1.2. Two Spikes

In this example the (non-isotropic) initial data describes two spikes, that are located symmetrically around the centre of the domain and are moving towards it. To simplify the simulation, we consider a constant chemoattractant concentration in the shape of a downwards opening parabola, which is fixed by setting the parameters within Equation (2.2) to zero. Therefore we have:

$$\begin{aligned}
\rho_+(0,x) &= 100 \exp\left(-\frac{(x+1)^2}{0.01}\right) + 10^{-4} \\
\rho_-(0,x) &= 100 \exp\left(-\frac{(x-1)^2}{0.01}\right) + 10^{-4} \\
q_+(0,x) &= 100 \exp\left(-\frac{(x+1)^2}{0.01}\right) \\
q_-(0,x) &= 100 \exp\left(-\frac{(x-1)^2}{0.01}\right) \\
m(0,x) &= -x^2 + 9
\end{aligned}$$

on the domain $[-3,3]$ with the parameters $\alpha = \frac{1}{2}$, $D_m = 0$, $\beta = 0$, $\delta = 0$, $\lambda = \frac{1}{2}$ and $s = 0$.
For the kinetic method, we use the initial data

$$\begin{aligned}
f(0,x,v) = &\frac{100}{0.05\sqrt{\pi}} \exp\left(-\frac{(v+1)^2}{0.01}\right) \exp\left(-\frac{(x-1)^2}{0.01}\right) \\
&+ \frac{100}{0.05\sqrt{\pi}} \exp\left(-\frac{(v-1)^2}{0.01}\right) \exp\left(-\frac{(x+1)^2}{0.01}\right).
\end{aligned}$$

In this example we want to compare the half-moment solution with the full-moment M_1 model whose initial condition can be obtained by setting $\rho = \rho_+ + \rho_-$ and $q = q_+ + q_-$.

We observe in Figure 5 that the two spikes move towards, collide in and then oscillate once around the centre of the domain until they reach a steady state forced by the constant chemoattractant concentration. In this case, there are noticeable differences in the closures. In the linear half-moment HP_1 model the density ρ takes negative values on the outer edge of the spikes, but these effects cancel out again after the collision in the centre of the domain. The full-moment minimum-entropy M_1 model wrongly predicts a lower speed of propagation when the two spikes hit each other, caused by the well-known "zero-netflux" problem of this model [20, 36]. In contrast, the speed of propagation predicted by the half-moment minimum-entropy HM_1 model is almost exact.

5.1.3. Kurganov Example

In this section we apply our simulation to an example described in [11] that produce bounded spiky steady states. This is of interest because it offers a model for cell aggregation which is a driving force behind embryological development and tumour formation.

[2] Dual Core 2.6 GHZ, 8 GB RAM

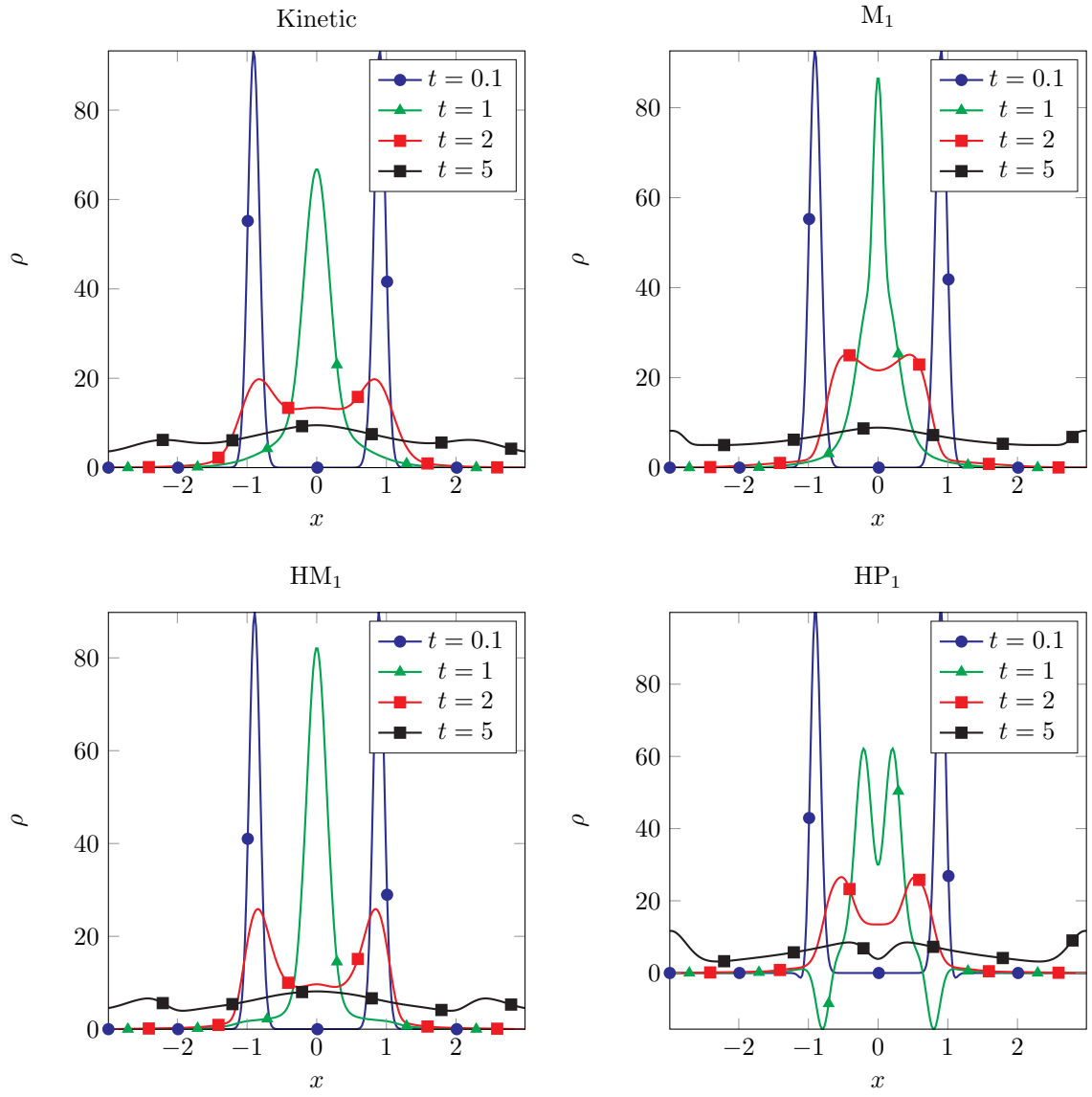

Figure 5: Comparison of models for the two-spikes example.

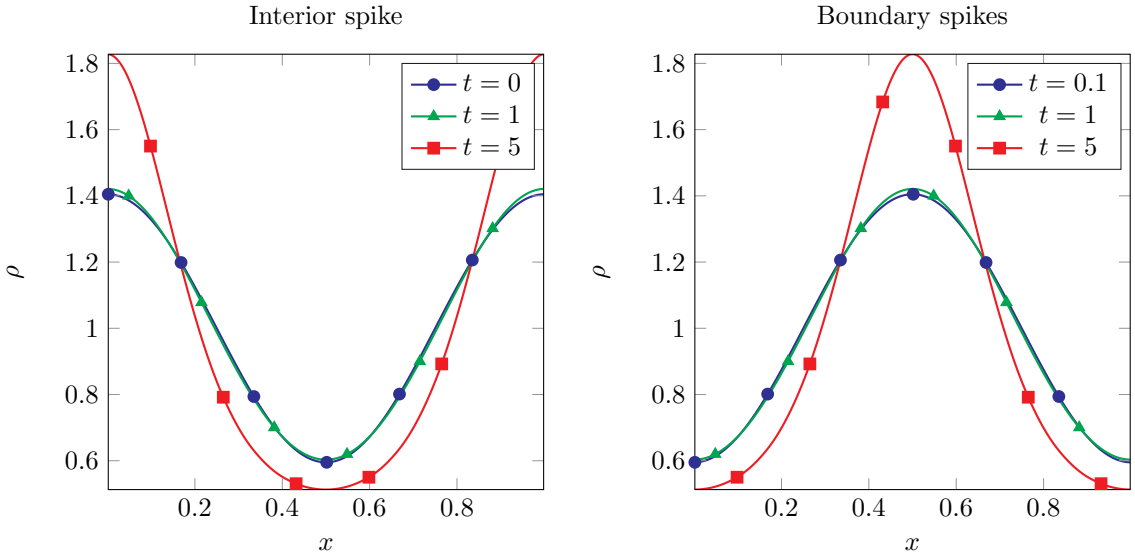

Figure 6: Half-moment minimum-entropy model for the Kurganov examples.

First, we use the initial data:

$$\rho_{\pm}(0,x) = \frac{1}{2}(1 - 0.01(1+4\pi^2)\cos(2\pi x))$$
$$m(0,x) = 1 - 0.01\cos(2\pi x)$$

on the domain $[0,1]$ with the parameters $\alpha = 1.2(1+4\pi^2)$, $D_m = 1$, $\beta = 1$; $\delta = 1$, $\lambda = \frac{1}{2}$ and $s = 0$. This produces an interior spike, while changing the sign to

$$\rho_{\pm}(0,x) = \frac{1}{2}(1 + 0.01(1+4\pi^2)\cos(2\pi x))$$
$$m(0,x) = 1 + 0.01\cos(2\pi x)$$

yields two boundary spikes. Since the results pictured in Figure 6 match those described in the paper [11], we omit the comparison to the results computed with the kinetic model here. We want to remark that in this case the M_1 model produces similar results.

5.2. Two dimensions

Finally, we transfer the One Spike and Two Spikes used in the one-dimensional case to two dimensions, which increases the complexity and highlights some advantages and disadvantages of the quarter-moment method. Unlike in one dimension, we do not have the means to compute a kinetic reference solution, but compare the results to those obtained with the full moment M_1 model [26, 28]. This model is well-known to be a good approximation to the true kinetic solution in many cases. All results are obtained on a grid with $\Delta x = \Delta y = 0.1$. By default, we will use isotropic initial conditions:

$$\rho_{\pm\pm'}(0,\mathbf{x}) = \int_{V_{\pm\pm'}} f(0,\mathbf{x},v)d\phi dr = \pi f(0,\mathbf{x}).$$

5.2.1. One Spike

Analogously to our first example in one dimension, we start by considering the simplest case of initial data: a single spike centred in the domain with no chemoattractant present. This is modelled by

$$\begin{aligned}\rho_{\pm\pm}(0,\mathbf{x}) &= \frac{1}{4}(100\exp(-100(x^2+y^2)+10^{-4})\\ m(0,\mathbf{x}) &= 0\end{aligned}$$

with $\mathbf{x} = (x,y)^T \in [-3,3]\times[-3,3]$ and the parameters $\alpha = 4$, $D_m = 1$, $\delta = 1$, $\beta = 8$,$\lambda = 2$ and $s = 0$.
Again, we observe in Figure 7 that the spike diffuses with decreasing speed. Just like in one dimension, switching between the exponential and linear closure relation has negligible effects.
The fact that the reference solution computed with the full-moment method pictured in Figure 8 is more flattened out is not surprising, since it uses the Lax-Friedrich scheme, which introduces more numerical dissipation. We also observe, that while the full-moment method conserves the rotational symmetry of the initial data, the quarter-moment method favours the axial directions, resulting in a more square-shaped solution. However, this effect vanishes for advancing times. Overall, this example shows that also in two dimensions, our simulation yields reliable results.

5.2.2. Two Spikes

Transferring the two-spikes example to two dimensions reveals a couple of interesting effects. Again, we use the initial data of two spikes that are located symmetrically around the centre of the domain and move towards it. In two dimensions though, we can consider different alignment of the spikes, strongly influencing the outcome. While in one dimension the spikes opposed each other, we chose to let them propagate on orthogonal paths. In the following we distinguish the cases of diagonal and axial placement of the spikes. To observe the effects of the simulation of Equation (2.1) more closely, we again turn off all dynamics of the chemoattractant by setting the parameters in (2.2) to zero. Diagonal placement of the spikes is modelled by the initial data

$$\begin{aligned}\rho_{+\pm}(0,\mathbf{x}) &= 10^{-4} & \rho_{-\pm}(0,\mathbf{x}) &= \zeta_\pm + 10^{-4}\\ q^x_{+\pm}(0,\mathbf{x}) &= 0 & q^x_{-\pm}(0,\mathbf{x}) &= -\frac{\zeta_\pm}{\sqrt{2}}\\ q^y_{+\pm}(0,\mathbf{x}) &= 0 & q^y_{-\pm}(0,\mathbf{x}) &= \pm\frac{\zeta_\pm}{\sqrt{2}}\\ m(0,\mathbf{x}) &= -(x^2+y^2)+18 & \zeta_\pm(0,\mathbf{x}) &= 100\exp(-\frac{(x-\frac{1}{\sqrt{2}})^2+(y\pm\frac{1}{\sqrt{2}})^2}{0.001})\end{aligned}$$

on the domain $[-3,3]\times[-3,3]$ with the parameters $\alpha = \frac{2}{\pi}$, $D_m = 0$, $\beta = 0$, $\delta = 0$, $\lambda = \frac{1}{\pi}$ and, $s = 1$. Similarly, the axial placement can be obtained by rotating the whole setup counter-clockwise by 45 degrees. Note that now, the initial distribution is no longer supported in the quarter spheres, e.g.

$$\rho_{--}(0,\mathbf{x}) = \frac{1}{2}(100\exp(-\frac{(x-1)^2+y^2}{0.001})+10^{-4}) + \frac{1}{2}(100\exp(-\frac{x^2+(y-1)^2}{0.001})+10^{-4}).$$

Since the full-moment M_1 model is rotationally invariant, we only consider the diagonal placement. The linearity of the kinetic equation (and the physical interpretation) suggests, that the two spikes should not influence each other, so we apply the full-moment model to initial data of the two spikes simultaneously and separately, superposing the two solutions to enforce the linearity. This is similar to a pencil-beam method, see e.g. [18]. Similar tests have been used in [26, 38] to investigate the M_1 and QM_1 model in case of fibre-laydown and radiative transfer equations. In the following we compare the results of those four computations: The simulation obtained by computing both spikes separately and then superposing the results acts as our reference and is pictured in Figure 9.

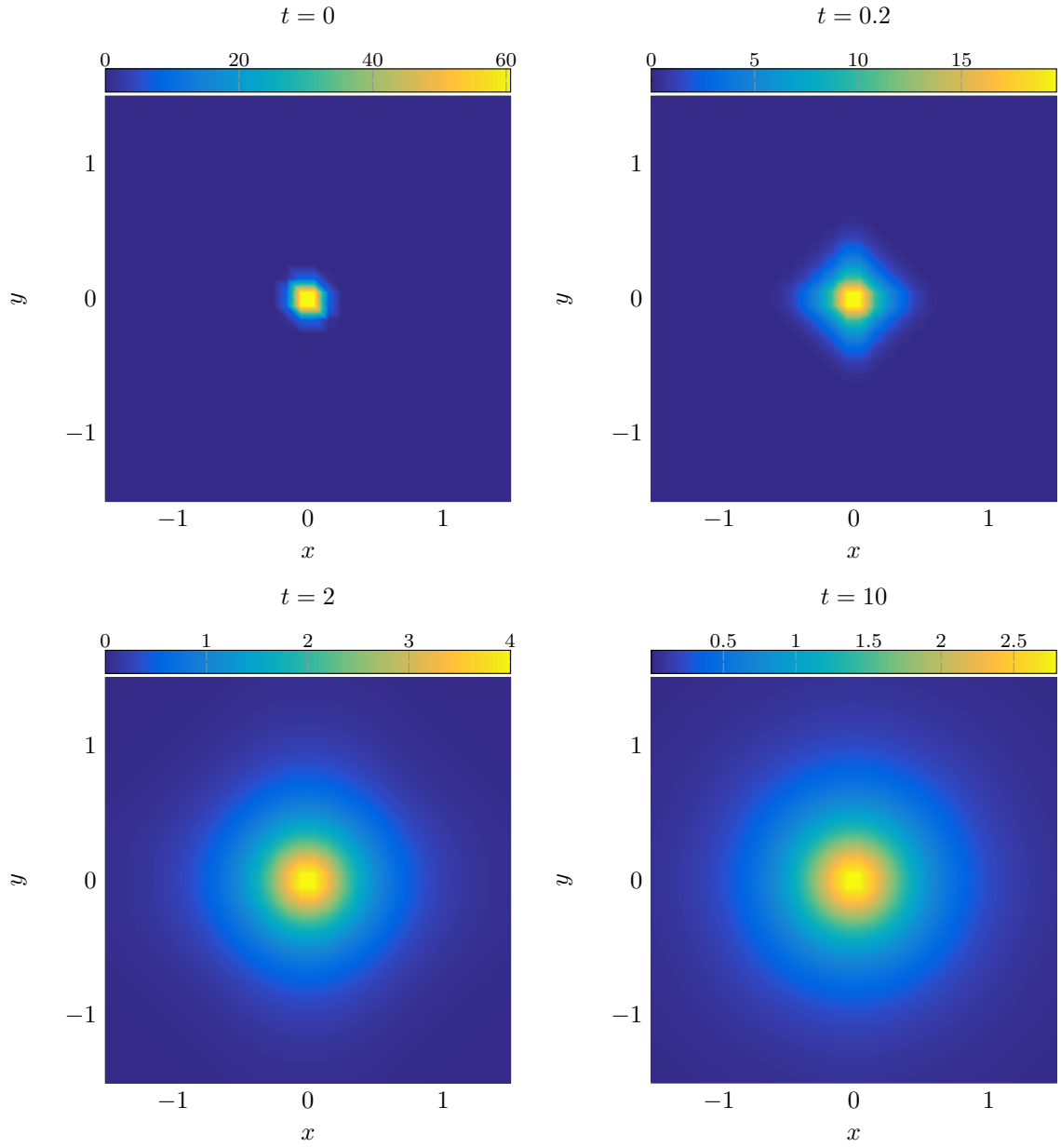

Figure 7: Quarter-moment QM_1 density ρ for the One Spike example.

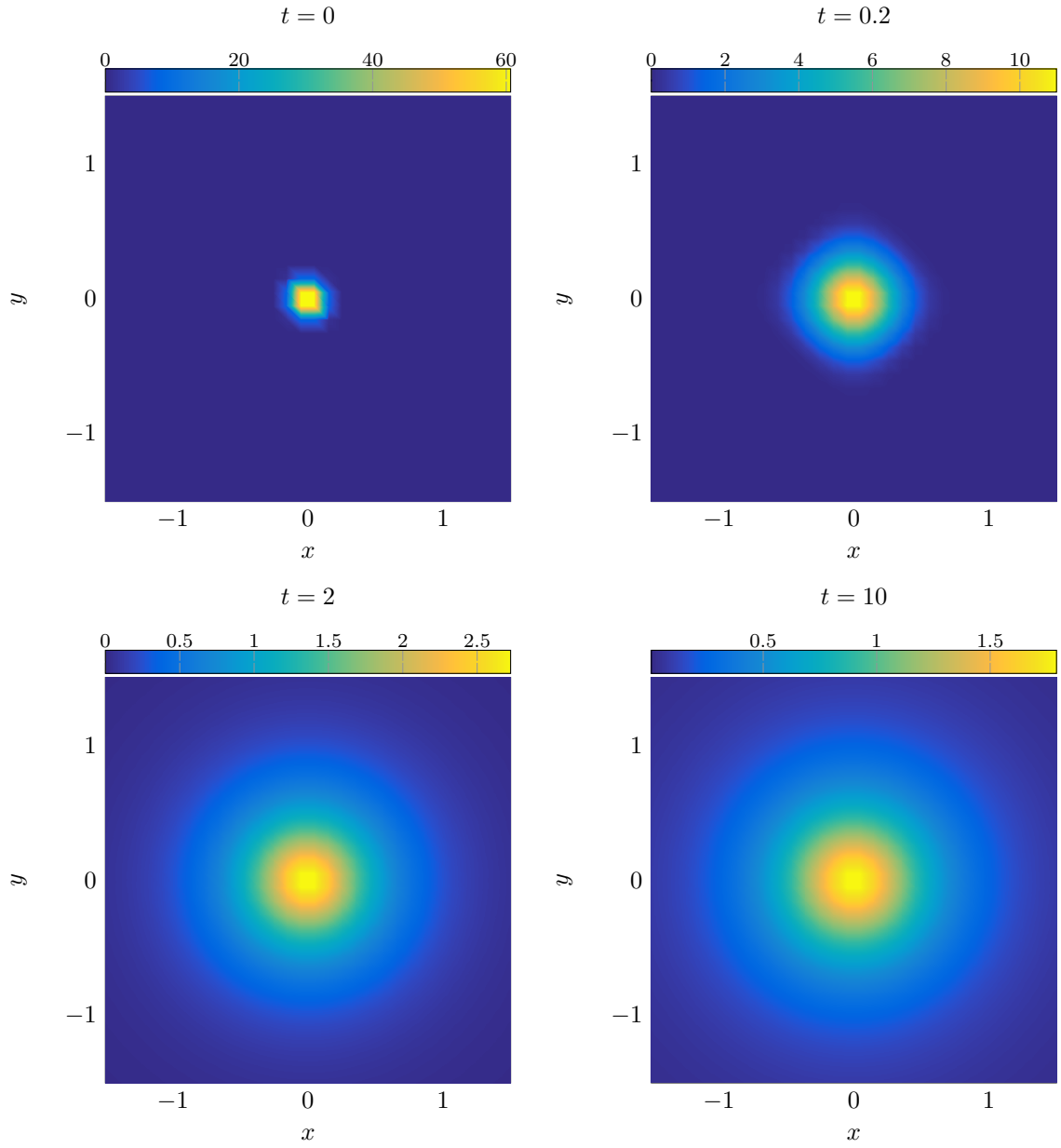

Figure 8: Full-moment M_1 reference density ρ for the One Spike example.

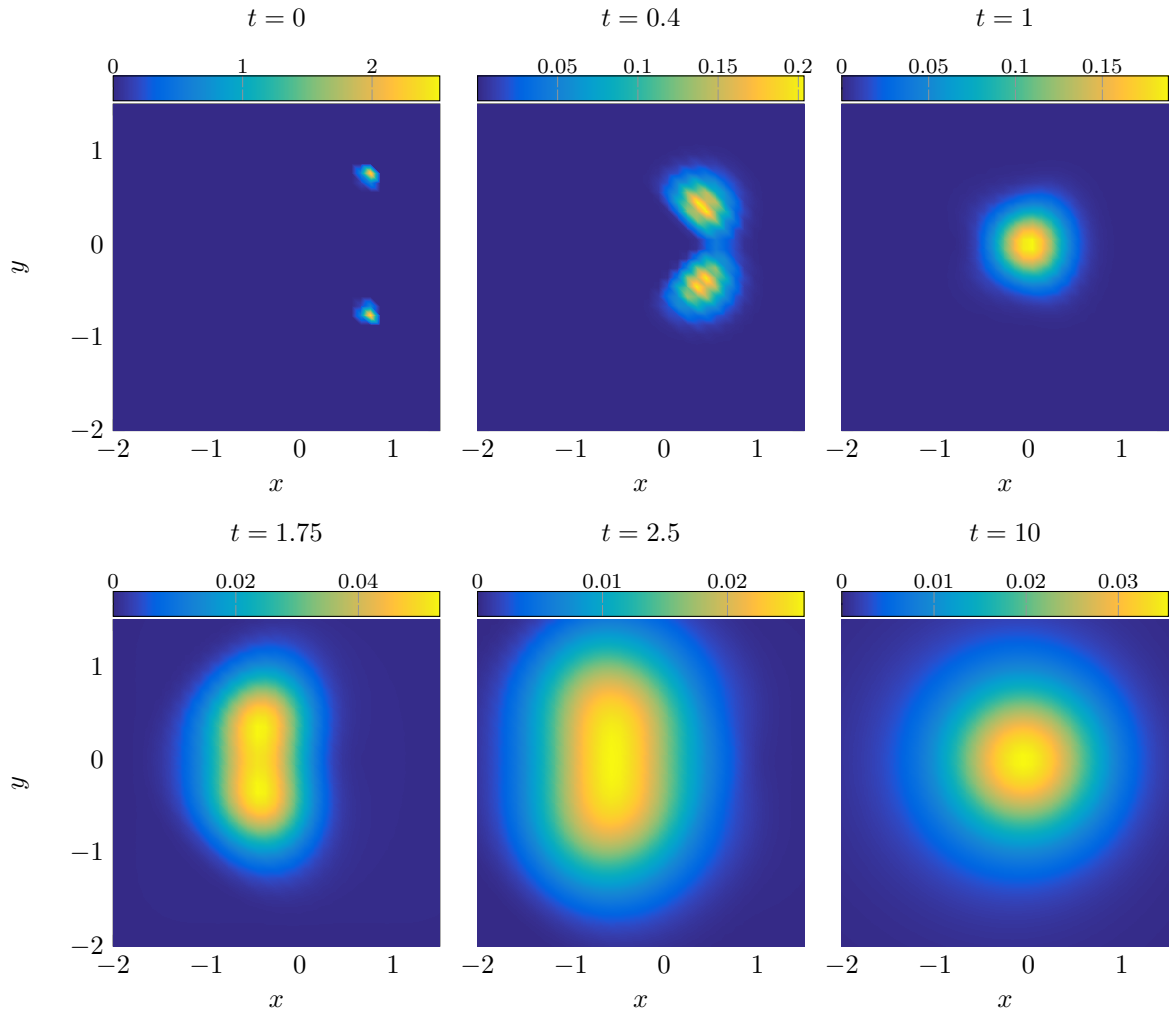

Figure 9: M_1 superposition of the two-spikes example with diagonal placement.

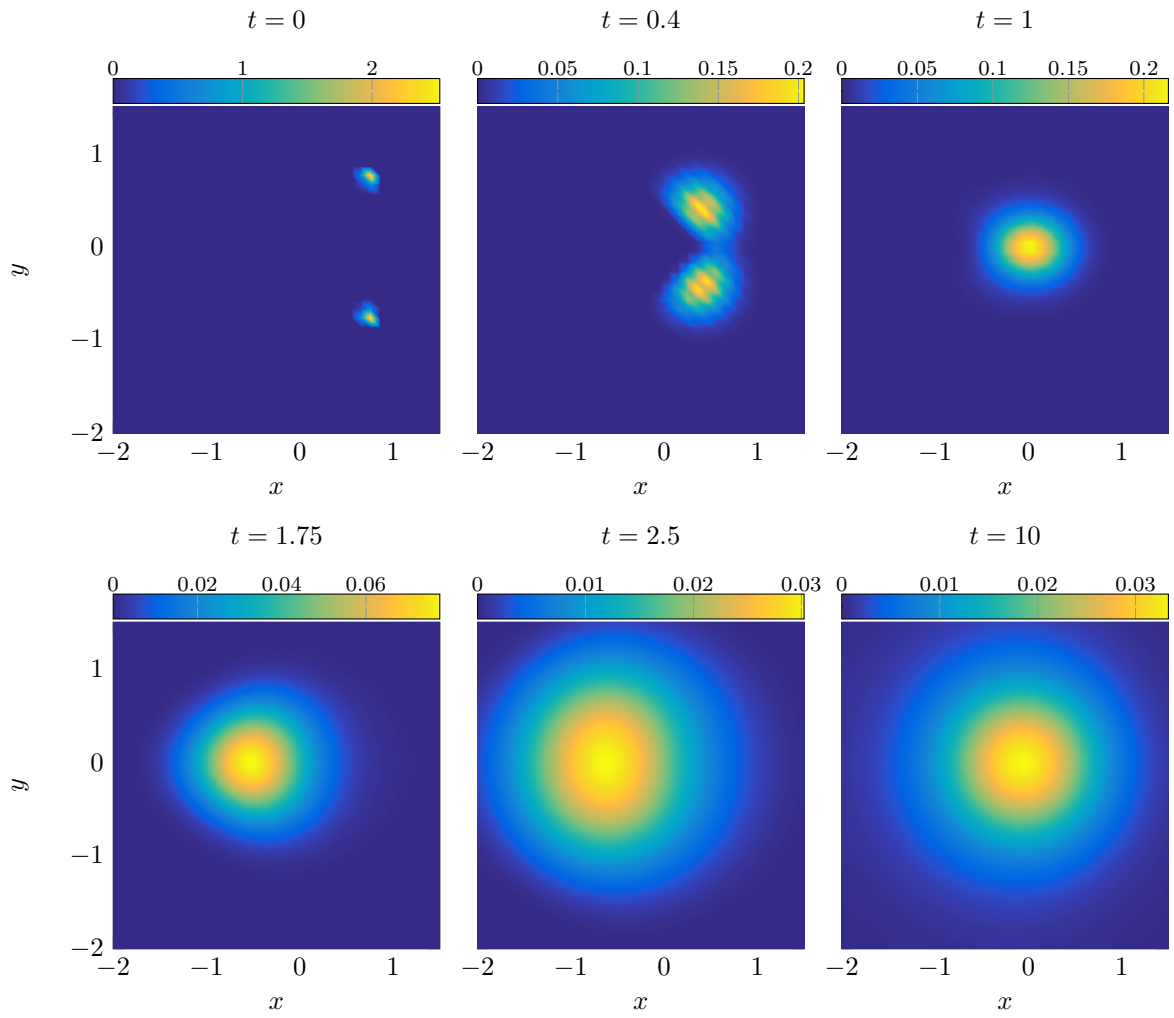

Figure 10: M_1 solution of the two-spikes example with diagonal placement.

It shows that the spikes move towards and then collide in the centre of the domain. They continue to move in their original directions but get pulled back towards the centre of the domain by the constant chemoattractant concentration, which forces a rotationally symmetric steady state. We observe that the full moment method applied to the full initial data visualised in Figure 10, does not produce the desired results. After colliding in the centre of the domain, the two spikes do not move on individually but rather as one before gravitating back towards the centre.

The results obtained by quarter-moment method with exponential closure are closer to the reference solution for the diagonal placement, see Figure 11, but not for the axial placement, see Figure 12.

These observations can be explained in the following way: The quarter-moment method operates on the quadrants of V and can therefore distinguish between the diagonally placed spikes whose velocities lie completely in V_{-+} and V_{--} respectively. Therefore they do not interfere, but rather superpose as desired. This does not work for the axial placement, since in this case both spikes contribute to ρ_{--}. The full-moment method can not distinguish between the two spikes at all, so we observe undesirable interference. This benchmark problem is also well suited to demonstrate the shortcomings of the linear QP_1 model. It is shown in Figure 13 that the particle density ρ can become negative, resulting in physically meaningless

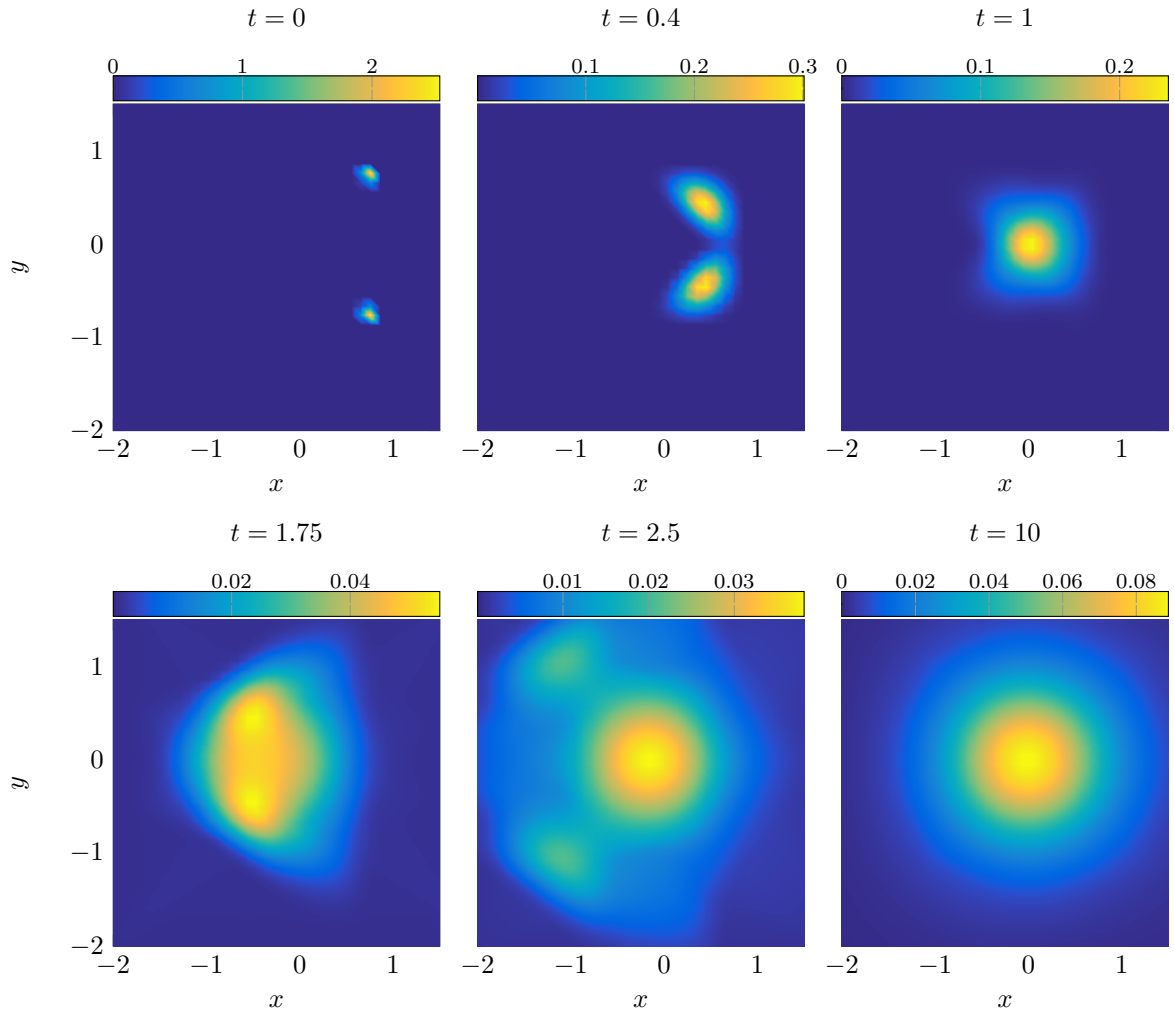

Figure 11: QM_1 solution of the two-spikes example with diagonal placement.

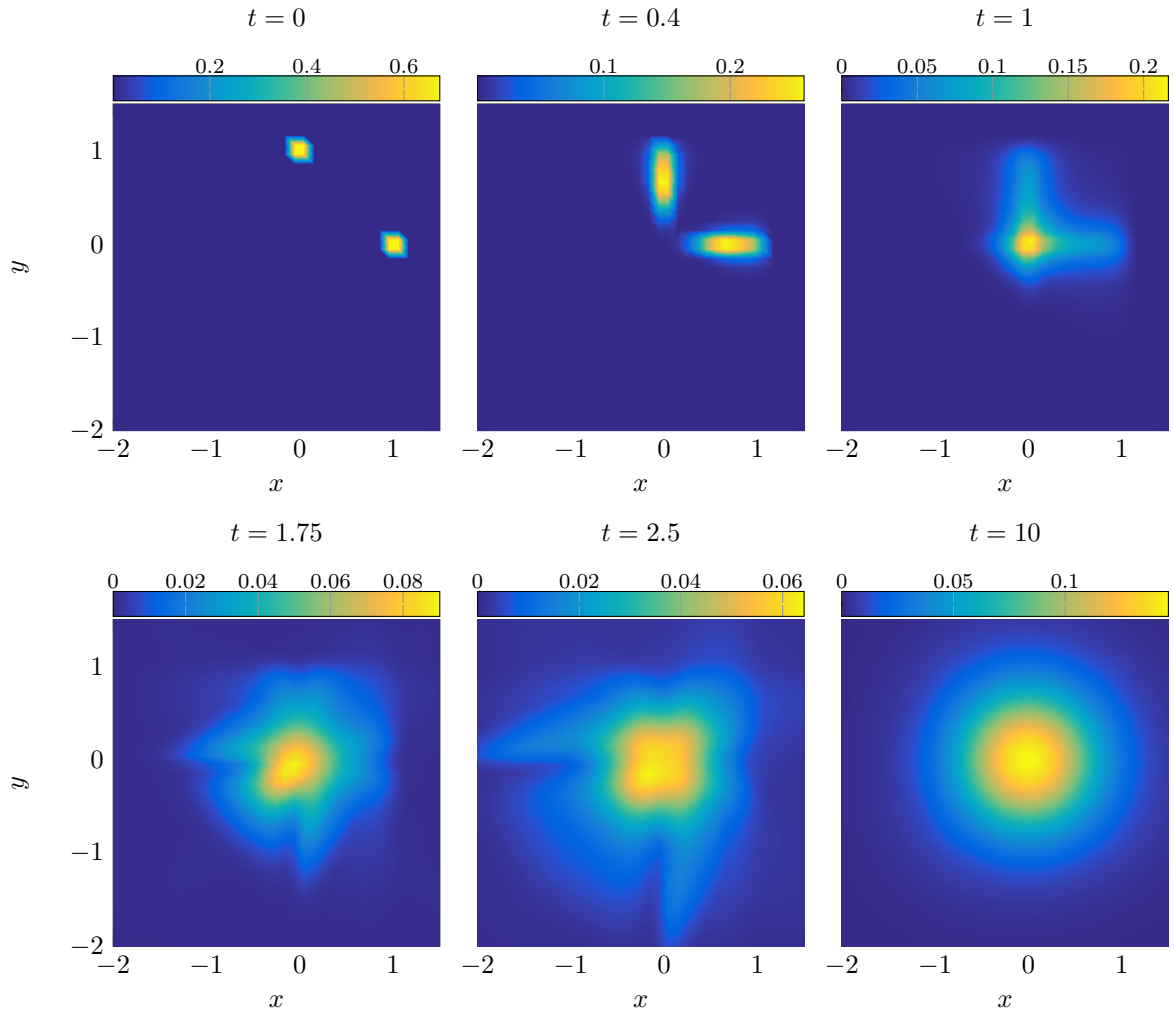

Figure 12: QM_1 solution of the two-spikes example with axial placement.

solutions.

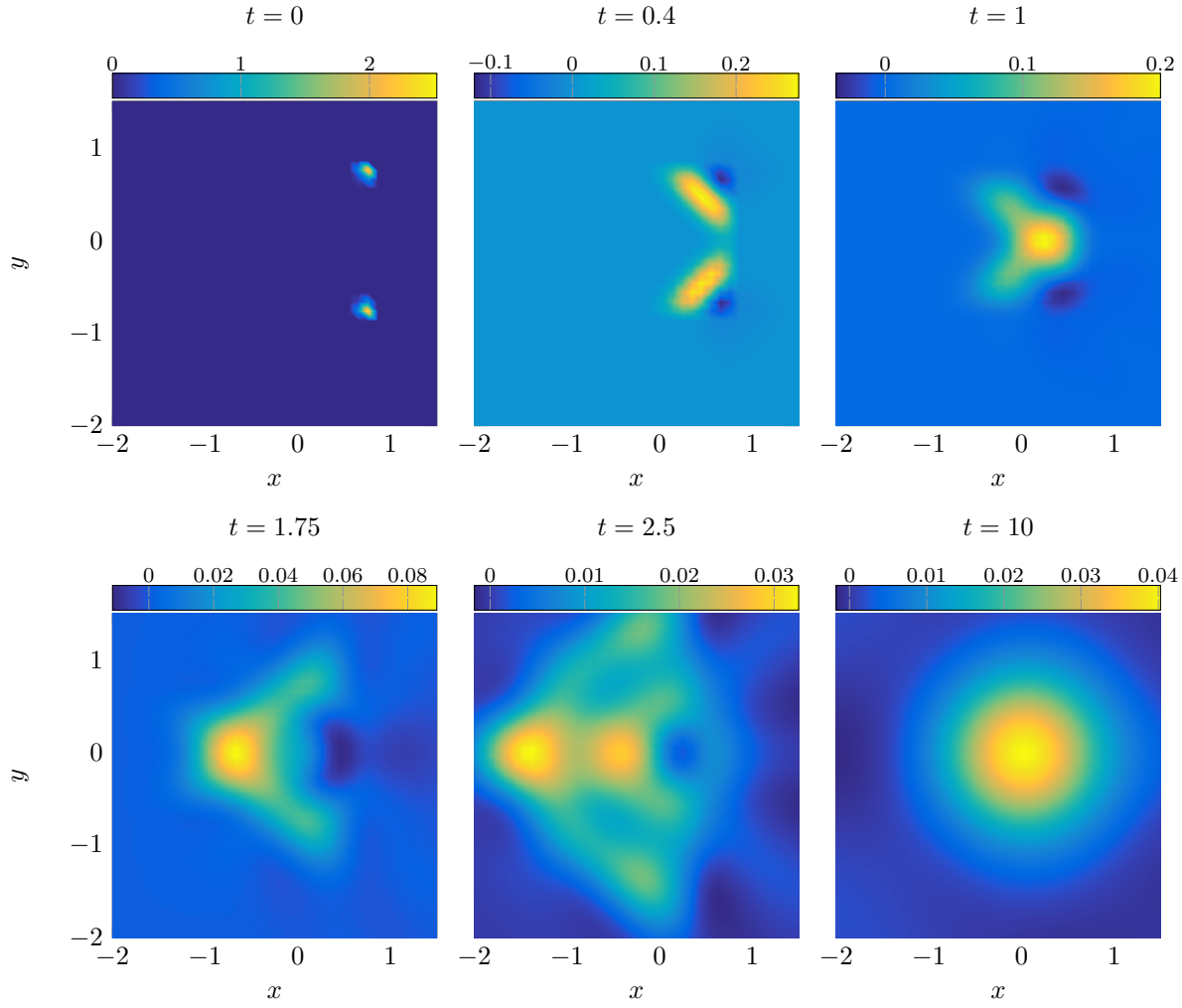

Figure 13: Results for Two Spikes example with diagonal placement using quarter-moment method, linear closure and $\Delta x = 0.1$

6. Conclusions

We have shown in various numerical experiments that the half-/ quarter-moment method yields macroscopic models that can produce satisfying simulations of chemotaxis using simple numerical schemes for partial differential equations. We have compared the results of the simulations in one dimension to those based on the kinetic equations and found that they give a good approximation while cutting down the computational expense considerably. Comparing the simulation results in two dimensions to those obtained with a full moment method has shown that the quarter-moment method is superior when dealing with non-isotropic initial data, but has its limitations caused by the geometry of the space of admissible velocities.

A typical strategy to solve this problem is to use higher-order models (full or partial moments). For example, the second-order M_2 model already provides reasonably better results in case of the two-dimensional two-spikes example (see e.g. [38] for a similar test case). However, although this model has less degrees of

freedoms (six equations in total while the QM_1 model has twelve) it is much more expensive. Due to the decoupling of the quarter-moment fluxes a two-dimensional tabulation strategy can be used. This is impossible in case of the M_2 model, which would require a five-dimensional tabulation. Thus, Newton-like algorithms have to be applied for the M_2 model in every space-time cell, leading to a high numerical cost, which is sometimes even more expensive than solving the kinetic equation itself.

A possibility to further increase the accuracy of the quarter-moment ansatz is to do a further refinement of the sphere, leading to a general first-order partial-moment model, which will hopefully converge to the true kinetic solution with a small number of refinements while being numerically efficient due to the inherent structure, still enabling a cheap tabulation strategy.

References

[1] W. Alt, *Orientation of cells migrating in a chemotactic gradient*, in Biological Growth and Spread, vol. 38 of Lecture Notes in Biomathematics, Springer Berlin Heidelberg, 1980, pp. 353–366.

[2] N. Bellomo, A. Bellouquid, J. Nieto, and J. Soler, *Multiscale biological tissue models and flux-limited chemotaxis for multicellular growing systems*, Mathematical Models and Methods in Applied Sciences, 20 (2010), pp. 1179–1207.

[3] N. Bellomo, A. Bellouquid, J. Nieto, and J. Soler, *On the asymptotic theory from microscopic to macroscopic growing tissue models: an overview with perspectives*, MMMAS, 22 (2012).

[4] N. Bellomo, A. Bellouquid, J. Nieto, and J. Soler, *Modeling chemotaxis from l2-closure moments in kinetic theory of active particles*, Discrete and Continuous Dynamical Systems Series B, 18 (2013), pp. 847–863.

[5] N. Bournaveas and V. Calvez, *The one-dimensional keller-segel model with fractional diffusion of cells*, Nonlinearity, 23 (2010), pp. 923–935.

[6] V. Calvez and J. A. Carrillo, *Volume effects in the keller–segel model: energy estimates preventing blow-up*, Journal de Mathematiques Pures et Appliquees, 86 (2006), pp. 155–175.

[7] F. Chalub, P. Markowich, B. Perthame, and C. Schmeiser, *Kinetic models for chemotaxis and their drift-diffusion limits*, Monatshefte fr Mathematik, 142 (2004), pp. 123–141.

[8] F. Chalub, P. Markowich, B. Perthame, and C. Schmeiser, *Kinetic models for chemotaxis and their drift-diffusion limits*, Monatsh. Math., 142 (2004), pp. 123–141.

[9] P. Chavanis, *Jeans type instability for a chemotactic model of cellular aggregation*, Eur. Phys. J. B, 52 (2006), pp. 433–443.

[10] A. Chertock, A. Kurganov, X. Wang, and Y. Wu, *On a chemotaxis model with saturated chemotactic flux*, Kinet. Relat. Models, 5 (2012), pp. 51–95.

[11] A. Chertock, A. Kurganov, X. Wang, and Y. Wu, *On a chemotaxis model with saturated chemotactic flux*, Kinetic and Related Models, 5 (2012), pp. 51–95.

[12] R. Curto and L. Fialkow, *Recursiveness, positivity, and truncated moment problems*, Houston J. Math, 17 (1991), pp. 603–636.

[13] B. Dubroca and A. Klar, *Half-moment closure for radiative transfer equations*, Journal of Computational Physics, 180 (2002), pp. 584–596.

[14] B. P. F. Filbet, P. Laurenot, *Derivation of hyperbolic models for chemosensitive movement*, J Math Biol., 50 (2005), pp. 189–207.

[15] M. Frank, *Partial Moment Entropy Approximation to Radiative Heat Transfer*, Pamm, 5 (2005), pp. 659–660.

[16] M. Frank, B. Dubroca, and A. Klar, *Partial moment entropy approximation to radiative heat transfer*, Journal of Computational Physics, 218 (2006), pp. 1–18.

[17] ———, *Partial Moment Entropy Approximation to Radiative Transfer*, (2006), p. to appear in J. Comput. Phys.

[18] M. Frank, H. Hensel, and A. Klar, *A fast and accurate moment method for the Fokker-Planck equation and applications to electron radiotherapy*, SIAM Journal on Applied Mathematics, 67 (2007), pp. 582–603.

[19] C. K. Garrett and C. D. Hauck, *A Comparison of Moment Closures for Linear Kinetic Transport Equations: The Line Source Benchmark*, Transport Theory and Statistical Physics, (2013).

[20] C. D. Hauck, *High-order entropy-based closures for linear transport in slab geometry*, Commun. Math. Sci. v9, (2010).

[21] M. A. Herrero and J. J. Velázquez, *A blow-up mechanism for a chemotaxis model*, Ann. Sc. Norm. Super. Pisa, Cl. Sci., IV. Ser., 24 (1997), pp. 633–683.

[22] T. Hillen, Hans, and G. Othmer, *The diffusion limit of transport equations derived from velocity jump processes*, Siam Journal on Applied Mathematics, 61 (2000), pp. 751–775.

[23] T. Hillen and K. Painter, *A user's guide to pde models for chemotaxis*, J. Math. Biol., 58 (2009), pp. 183–217.

[24] E. F. Keller and L. A. Segel, *Initiation of slime mold aggregation viewed as an instability*, J. Theor. Biol., 26 (1970), pp. 399–415.

[25] ———, *Model for chemotaxis*, Journal of Theoretical Biology, 30 (1971), pp. 225–234.

[26] A. Klar, F. Schneider, and O. Tse, *Approximate models for stochastic dynamic systems with velocities on the sphere and associated Fokker–Planck equations*, Kinetic and Related Models, 7 (2014), pp. 509–529.

[27] C. D. Levermore, *Relating Eddington factors to flux limiters*, Journal of Quantitative Spectroscopy and Radiative Transfer, 31 (1984), pp. 149–160.

[28] ———, *Relating eddington factors to flux limiters*, Journal of Quantitative Spectroscopy and Radiative ..., 31 (1984), pp. 149–160.
[29] ———, *Moment closure hierarchies for kinetic theories*, Journal of Statistical Physics, 83 (1996), pp. 1021–1065.
[30] E. E. Lewis and J. W. F. Miller, *Computational Methods in Neutron Transport*, John Wiley and Sons, New York, 1984.
[31] MATLAB, *version 8.5.0.197613 (R2015a)*, The MathWorks Inc., Natick, Massachusetts, 2015.
[32] R. Natalini, *Hyperbolic models of cell movements: an introduction.*
[33] M. Rascle and C. Ziti, *Finite time blow-up in some models of chemotaxis*, J. Math. Biol., 33 (1995), pp. 388–414.
[34] J. Ritter, *Macroscopic Models for Cell Migration*, bachelor thesis, Technische Universität Kaiserslautern.
[35] M. Schäfer, M. Frank, and R. Pinnau, *A hierarchy of approximations to the radiative heat transfer equations: modelling, analysis and simulation*, Mathematical Models and Methods in Applied Sciences, 15 (2005), pp. 643–665.
[36] F. Schneider, G. W. Alldredge, M. Frank, and A. Klar, *Higher Order Mixed-Moment Approximations for the Fokker–Planck Equation in One Space Dimension*, SIAM Journal on Applied Mathematics, 74 (2014), pp. 1087–1114.
[37] F. Schneider, G. W. Alldredge, and J. Kall, *A realizability-preserving high-order kinetic scheme using WENO reconstruction for entropy-based moment closures of linear kinetic equations in slab geometry*, Kinetic and Related Models, (2015).
[38] F. Schneider, J. Kall, and A. Roth, *First-order quarter- and mixed-moment realizability theory and Kershaw closures for a Fokker-Planck equation in two space dimensions*, (2015).
[39] M. Tindall, P. Maini, S. Porter, and J. Armitage, *Overview of mathematical approaches used to model bacterial chemotaxis ii: Bacterial populations*, Bulletin of Mathematical Biology, 70 (2008), p. 15701607.
[40] E. F. Toro, *Riemann Solvers and Numerical Methods for Fluid Dynamics*, Springer London, Limited, 2009.